DOI:10.28974/idojaras.2022.2.3

IDŐJÁRÁS

Quarterly Journal of the Hungarian Meteorological Service
Vol. 126, No. 2, April – June, 2022, pp. 203–232

Spatial effect of anti-COVID measures on land surface temperature (LST) in urban areas: A case study of a medium-sized city

Kamill Dániel Kovács* and **Ionel Haidu**

Université de Lorraine
Laboratoire LOTERR-EA7304
Île du Saulcy, 57045 Metz, France

**Corresponding author E-mail: kamill-daniel.kovacs@univ-lorraine.fr*

(Manuscript received in final form March 1, 2021)

Abstract— This case study investigates the magnitude and nature of the spatial effect generated by the anti-COVID measures on land surface temperature (LST) in the city of Târgu Mureș (Marosvásárhely), Romania. The measures were taken by the Romanian government during the state of emergency (March 16 – May 14, 2020) due to the SARS-CoV-2 coronavirus pandemic. The study shows that – contrary to previous studies carried out on cities in China and India – in most of the urban areas of Marosvásárhely LST has increased in the period of health emergency in 2020 concerning the large average of the years 2000–2019. Remote sensing data from the MODIS and the Landsat satellites show, that MODIS data, having a moderate spatial (approximately 1 km) but good temporal resolution (daily measurements), show a temperature increase of +0.78 °C, while Landsat data, having better spatial (30 m) but lower temporal resolution, show an even greater increase, +2.36 °C in the built-up areas. The difference in temperature increase is mainly due to the spatial resolution difference between the two TIR band sensors. The LST anomaly analysis performed with MODIS data also shows a positive anomaly increase of 1 °C. However, despite this increase, with the help of the hotspot-coldspot analysis of the Getis-Ord Gi* statistic we were able to identify 46 significant coldspots that showed a 1–2 °C decrease of LST in April 2020 compared to the average of the previous years in April. Most of these coldspots correspond to factory areas, public transport epicenters, shopping centers, industrial polygons, and non-residential areas. This shows that anti-COVID measures in the medium-sized city of Marosvásárhely had many effects on LST in particular areas that have links to the local economy, trade, and transport. Paired sample t-test for areas identified with LST decrease shows that there is a statistically significant difference in the average LST observed before and after anti-COVID measures were applied. MODIS-based LST is satisfactory for recognizing patterns and trends at large or moderate geographical scales. However, for a hotspot-coldspot analysis of the urban heat islands, it is more suitable to use Landsat data.

Key-words: LST, TIR band, thermal sensor, anti-COVID measures, spatial effect, urban heat islands, medium-sized city, hotspot-coldspot analysis, Getis-Ord Gi*, QGIS

1. Introduction

Space remote sensing is a technology that has undergone constant progress in recent years. Nowadays it is one of the methods for change analysis by studying the events that occur in the Earth's spheres. It allows the obtaining of several geophysical magnitudes and variables that are within the geographic space. Thermal remote sensing is a branch of spatial remote sensing that studies the Earth's temperature. This is done by measurements obtained by a sensor onboard a satellite platform or an aircraft containing a TIR (thermal infrared) band. This sensor measures the electromagnetic radiation emitted by the Earth's surface in the thermal infrared region of the electromagnetic spectrum (between 8 and 14 μm) emitted by the Earth's surface and atmosphere (*Sobrino et al.,* 2000). Therefore, land surface temperature (LST) allows us to indirectly study the qualitative and quantitative processes that occur on the Earth's surface, and thus, to analyze and model changes over time (*Quattrochi* and *Luvall*, 2004; *Kovács*, 2019; *Ursu*, 2019; *Kis et al.,* 2020).

Previous studies have shown that LST has experienced significant declines during the emergency of COVID-19 in cities of China and India, where strict quarantine policy measures were adopted. *Maithani et al.* (2020) has pointed out that areas with high building density had minimal LST decline, while large proportions of open spaces with medium or low building density had maxima LST declines. *Hadibasyir et al.* (2020), in their study on Wuhan city, China, have shown that during the COVID-19 emergency with applied policies of breaking the virus spread, LST was lower than the average of the last three years on the same dates. However, in these two cases large cities were studied that have greater impact on their environment than the medium-sized cities or small towns.

Other studies also addressed the effects of COVID-19 concerning changes detected in the environment (*Liu et al.,* 2020; *Tobías et al.,* 2020; *Xie* and *Zhu*, 2020; *Lin et al.,* 2020; *Ma et al.,* 2020; *Awasthi et al.*, 2021; *Agrawal et al.,* 2020; *Singh et al.,* 2020; *Patel et al.,* 2020). LST has a principal part in climate change topics, because directly or indirectly, land surface temperature influences other factors related to hydrology, agriculture, or the urban environment (*Avdan* and *Jovanovska Kaplan*, 2016). Researchers also describe that anthropogenic factors, in general, can have a significant effect on LST (*Buyantuyev* and *Wu*, 2010; *Li et al.,* 2016; *Meng* and *Dou,* 2016). Factors such as urbanization, general transport, large centers of public transport, industrial and residential activities are related to LST (*Yoo et al.,* 2017; *Wang et al.,* 2017).

The alterations in LST that occur in urban areas are mainly depending on the characteristics of the materials that form the buildings, orientation, density of buildings, and also there is the main factor of anthropogenic heat sources generated near the surface (*Maithani et al.,* 2020; *Zsebeházi* and *Szépszó,* 2020). With all this, the result is that the LST in urban areas is altered, modified artificially in contrast to the non-built-up areas. This is how the phenomenon of

urban heat islands (UHI) appears *(Mathew et al.,* 2016; 2017; *Mukherjee et al.,* 2017; *Kikon et al.,* 2016; *Mallick et al.,* 2013; *Xu et al.,* 2012; *Imhoff et al.,* 2010; *Yuan* and *Bauer*, 2007; *Gallo et al.,* 1993; *Oke,* 1982).

With the help of remote sensing technology, by calculating LST, we can identify these heat islands and their changes in the urban environment. Therefore, these changes indirectly explain the effects of human activities within the urban environment.

This study analyzes the changes in land surface temperature that have occurred within the urban area of the city of Marosvásárhely in the reference period of March 16 –May14, 2020. The study compares and detects the changes that occurred in 2020 compared to a large average of the previous years between 2000–2019. The state of emergency in Romania due to the pandemic of SARS-CoV-2, a new respiratory disease, was declared on March 14, 2020, implemented on March16, and extended on April 15 by 30 days until May 14, by a government decree. The main measures adopted were the cancellation of classes at the pre-university and university levels, limitation of public transport, compulsory wearing of masks in enclosed spaces, partial limitation of mobility of persons (permitted only with a personal statement and indicating the purpose of the posting).

2. Study area and data

Târgu Mureș (Marosvásárhely) is the main town in the district of Mureș (Maros) in the historical region of Transylvania, Romania (46°32’44’’N 24°33’45’’E) (*Fig. 1*). According to the latest Romanian census (*Institutul Național de Statistică,* 2011), it has a population of 134,290 inhabitants, an area of 49.3 km^2, making it the 16th largest city in the country. It extends along the two banks of river terraces of the River Mureș (Maros). At the country level, it is an important center of the chemical industry (Azomureș), and also of pharmaceutical, textile, wood, and food industries.

The data used for calculating the surface temperature are remote sensing data from the MODIS and Landsat satellite sensors. Remote sensing technology makes LST measurements possible by satellites in different orbits, on a multi-temporal scale. However, these satellites provide data in different spatial and temporal resolutions (*Maithani et al.,* 2020; *Jensen,* 2015; *Ndossi* and *Avdan,* 2016).

LST data from two different sensors (MODIS and Landsat) have used in this study. The reason for choosing this method is to find the balance between the spatial and temporal resolution of the available data. MODIS/MOD11A1 provides daily LST data with a spatial resolution of approximately 1 km. MODIS/MOD11A2, in turn, provides data of an average of 8 days with the same spatial resolution. Instead, Landsat sensors provide data with a much better spatial resolution (30 m). The Landsat 4–5 TIR band (band 6,10.40 – 12.50 μm) obtains

data at 120 m resolution, but it is resampled to 30 m. Landsat 7 band 6 (10.40 – 12.50 µm) acquires data at 60 m resolution, then it is resampled to 30 m. Landsat 7 acquires thermal data in two different bands (band 6H - high gain, band 6L - low gain). The gain difference is present, because it is essential for studies of different types and purposes.

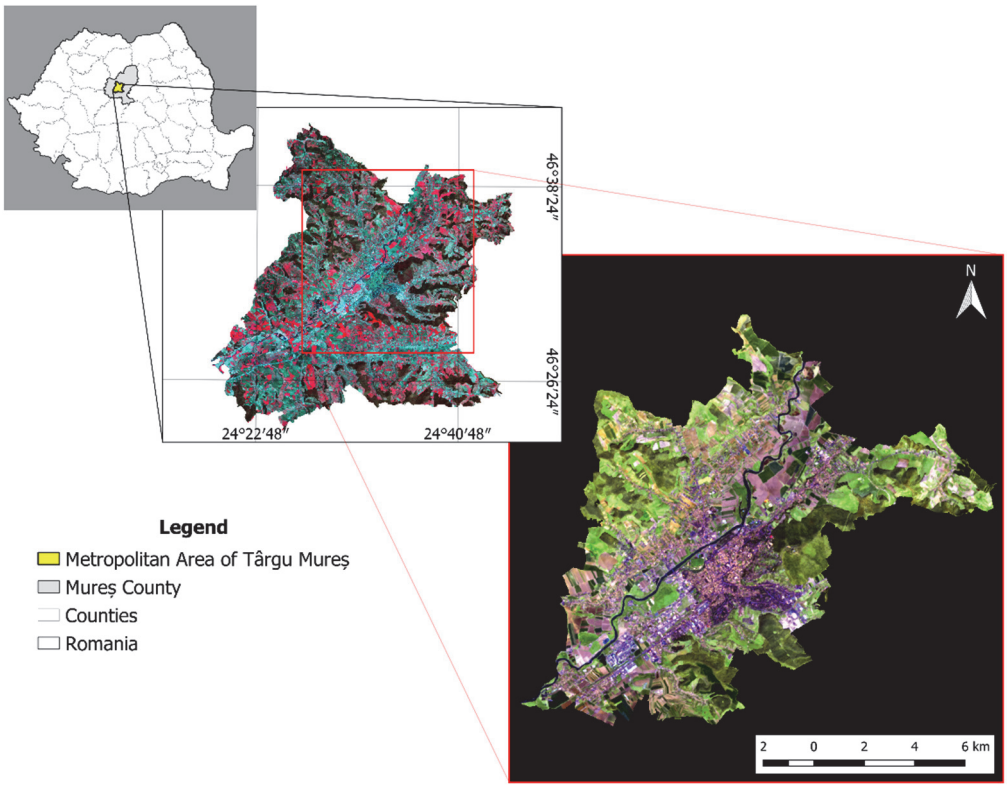

Fig. 1. Location of the functional urban area of Târgu Mureș (Marosvásárhely).

In this study, we have used band 6H (BAND_6_VCID_2), which has a higher radiometric resolution (sensitivity), a more restricted dynamic range, and is more likely to become saturated on hot objects. The reason for this choice is that the high gain setting is better for scenes that are in temperate zones, areas that have a lower surface luminosity, because the high gain has a temperature range between 240–320 K (*Karnieli et al.,* 2004; *Barsi et al.,* 2006; *Slater et al.,* 1987; *Donegan* and *Flynn,* 2004). Landsat 8 has two thermal infrared bands (TIRS): band 10 (10.60–11.19 µm) and band 11 (11.50–12.51 µm). In this study, we have used band 10, which is better in the calculation of current evapotranspiration, since it measures with high gain, while band 11 provides low gain (*Xu,* 2015; *Du et al.,* 2015; *Yu et al.,* 2014; *Xiao et al.,* 2007; *Rozenstein et al.,* 2014; *Sahana et al.,* 2016).

As we saw above, MODIS LST data has a lower spatial resolution (1 km) than Landsat (30 m). However, MODIS obtains daily data. Despite this, the

MODIS LST calculation continues to improve the cloud pollution removal, the update of the look-up table coefficient (LUT) for the split-window algorithm, and the classification to obtain emissivity. Also, studies have tested with ground validation methods that MODIS LST data show dependable accuracy (*Eleftheriou et al.,* 2018; *Hulley et al.,* 2012). On the other hand, the difficulty with using Landsat data is that they have a fairly long return period. Besides, from March to May (spring), in the temperate zones, such as where Marosvásárhely is located, clouds are more frequent in the scenes. Therefore, the effective temporal resolution (i.e., satellite images that can be used in the study period) can be greatly reduced. For this reason, we chose to use both MODIS LST and Landsat LST data to compare land surface temperature results. We have seen that the overall comparison results between 2020 and the long average of the years 2000–2019 of MODIS are corroborated with the results of Landsat and, knowing this, we have used the data of Landsat for the most in-depth analyses (hotspot-coldspot change detection analysis).

The Landsat data used are presented in *Table 1*. In the case of Landsat data, the reference date is a scene from the emergency period, which is April 8, 2020. Other satellite scenes have been searched in the previous years in the month of April with a maximum difference of 6 days to reduce the effect of the natural cycle of LST.

Landsat's NIR and RED bands have been downloaded from the Collection 2 Level 2 database, where the atmospheric effects on products are corrected. This step is crucial, because if the surface emissivity is calculated from the normalized vegetation index, on NIR and RED bands must be corrected atmospheric effects (*Dissanayake et al.,* 2019a, 2019b; *Ranagalage et al.,* 2018; *Sekertekin* and *Bonafoni,* 2020).

Table 1. Landsat data used

Landsat	Date	Difference from reference
L8	April 8, 2020	*reference*
L7	April 11, 2018	3 days
L7	April 5, 2016	3 days
L8	April 11, 2015	3 days
L8	April 8, 2014	0 days
L7	April 10, 2012	2 days
L5	April 13, 2010	5 days
L7	April 13, 2007	5 days
L7	April 7, 2005	1 day
L7	April 4, 2004	4 days
L7	April 2, 2003	6 days

TIR bands have been downloaded from Level 1 products, because in this study, LST was calculated with the radiative transfer equation (RTE), and this equation requires that the TIR band must be in digital numbers (DN) (0-255). Vector data referring to the boundaries of different urban area categories and administrative boundaries are derived from the Urban Atlas data of the Copernicus Programme. Data processing and obtaining the results were carried out with open source softwares Google Earth Engine and QGIS.

3. Techniques and methodology

There are different methods and algorithms for extracting LST from the TIR band (*Jiménez-Muñoz et al.,* 2014; *Sattari* and *Hashim,* 2014; *Mohamadi et al.,* 2019; *Hulley et al.,* 2019; *Dousset et al.,* 2019; *Weng,* 2019; *Vlassova et al.,* 2014; *Soleimani Vosta Kolaei* and *Akhoondzadeh,* 2018). This procedure is based on the inversion of the Planck's law and the brightness temperature obtained from the atmospheric radiance from the TIR band sensor (*Mathew et al.,* 2016).

The surface emissivity is also calculated, then these parameters along with the calibration coefficients are entered into an equation that calculates the LST estimation values. Other atmospheric corrections are also generally applied. The radiative transfer equation (RTE) has been used in this study to obtain the LST values (*Mallick et al.,* 2012; *Yu et al.,* 2014; *Wang* and *Upreti,* 2019; *Sobrino et al.,* 2004; *Sobrino* and *Romaguera*, 2004). The reference period of the study is March 16 – May 14. This period is analyzed in 2020 and in the previous years too (2000–2019). The reference period of 2020 has been chosen for all previous years to 2020 according to the health emergency period in 2020. This type of research should compare not only the LST variation before and after anti-COVID measures have been applied but also the LST in previous years in the same period of the year, thus avoiding the influence of regular changes of seasons of the year. The techniques and methodology of the study are detailed below.

3.1. LST extraction from MODIS data

MODIS11A2 and MODIS11A1 LST data were created based on a generalized split-window algorithm under cloud-free conditions (*Wan,* 2013; *Duan et al.,* 2019). The digital number (DN) values of MOD11A2 and MOD11A1 were calibrated to LST values in Kelvin scale by multiplying the DN with 0.02. From the obtained results, 273.15 were subtracted, thus the LST values in degrees Celsius were finally obtained. This whole process was done in Google Earth Engine using lines of JavaScript code.

The monthly temperature anomaly was calculated with MOD11A2 data with the following equation (*Ceccato et al.,* 2017):

$$r'_{ij} = r_{ij} - \frac{1}{N_i}\sum_{j=1}^{N} r_{ij}, \quad (1)$$

where *r'ij* is the monthly anomaly, *rij* is the original monthly value, and the rest of the equation is the calculation of the monthly climatology, which is subtracted from the original monthly values.

According to *Ceccato et al.* (2017), in climatology, anomaly means the difference between the value of a quantity and its mean climatological value. A monthly anomaly is a difference between the original monthly value of an amount in a given month and the monthly climatological value for that month of the year.

3.2. LST extraction from Landsat data

The authors have developed an automated processing model in QGIS Graphical Modeller for calculating the LST with Landsat satellite images. For Landsat 8, 7, and 5 products, three different models have been built, respectively. The difference between these models is that for Landsat 7 satellite images, a correction process of the gaps produced by the sensor's technique issue has been implemented in the model process, while for the other Landsat scene products, this step is not required (nor for Landsat 7 products before June 2003). In all models, cloud pixels have been excluded by identifying clouds with the BQA band of Level 1 by applying threshold values.

3.2.1. Vegetation indices and emissivity

The problem with estimating the Earth's surface temperature with satellite data are the effects appear due to atmospheric absorption and surface emissivity. For the emissivity calculation, we have used the model presented by *Valor* and *Caselles* (1996). NIR and RED bands have been used which are atmospherically corrected (Level 2). NDVI has been calculated as follows (*Sellers,* 1985):

$$NDVI = \frac{(NIR-RED)}{(NIR+RED)}. \quad (2)$$

Based on the NDVI index, the vegetation proportion index (Pv) has been calculated. This calculation is necessary to isolate the thermal emissivity of the vegetation. These values (max and min NDVI) are taken as reference values (*Valor* and *Caselles*, 1996):

$$Pv = \left(\frac{(NDVI-NDVI_{min})}{(NDVI_{max}-NDVI_{min})}\right)^2. \quad (3)$$

This result is the basis for the calculation of emissivity. A typical value for vegetation in thermal infrared is 0.99. However, choosing a typical emissivity

value for another type of soil is more complicated. We have taken the proposed value from 49 samples as reference from the Aster spectral library. In this case, the mean value is 0.986 with a standard deviation of 0.004:

$$\varepsilon = 0.004 * Pv + 0.986\,. \tag{4}$$

3.2.2. DN conversion to radiance

Landsat 7 and 5 data were converted to radiance using the spectral radiance scale method:

$$L_\lambda = \left(\frac{LMAX_\lambda - LMIN_\lambda}{Qcalmax - Qcalmin}\right) * (Qcal - Qcalmin) + LMIN_\lambda\,, \tag{5}$$

while Landsat 8 data were converted to radiance using the gain and bias method:

$$L_\lambda = ML * Qcal + AL\,, \tag{6}$$

where

$$ML = \left(\frac{LMAX_\lambda - LMIN_\lambda}{Qcalmax - Qcalmin}\right), \tag{7}$$

$$AL = LMIN_\lambda - \left(\frac{LMAX_\lambda - LMIN_\lambda}{Qcalmax - Qcalmin}\right) * Qcalmin\,. \tag{8}$$

In Eqs. (5–8), L_λ is the spectral radiance in the sensor (satellite radiance), *ML* is the band-specific reset multiplicative factor from the metadata (RADIANCE_MULT_BAND_x, where x is the band number), *AL* is the band-specific reset additive factor from the metadata (RADIANCE_MULT_BAND_x, where x is the band number), *Qcal* is the discretized and calibrated pixel values of the standard product (DN digital values), $LMAX_\lambda$ is the maximum spectral radiance corresponding to the band *Qcalx,* $LMIN_\lambda$ is the minimum spectral radiance corresponding to the band *Qcalx, Qcalmax* is the maximum pixel value depending on the radiometric resolution, *Qcalmin* is the minimum pixel value.

The problem with the transformation of radiance to land surface temperature is that dispersion and atmospheric transmission (effects produced by albedo and water vapor) alter values and give temperature values that do not correspond to the ground. For correcting these effects, a corrected radiative transfer equation has been used by applying it to the radiance obtained with the above equations (*Coll et al.,* 2010):

$$B(T) = \frac{L_{sen} - L^{\uparrow}}{\varepsilon\tau} - \frac{1-\varepsilon}{\varepsilon} L^{\downarrow}\,, \tag{9}$$

where L_{sen} is the radiance measured by the sensor ($W/m^{-2}/sr^{-1}/\mu m^{-1}$), ε is the emissivity of the surface, B is the parameter derived from the Planck's law calculated from the surface temperature calculation equation (°K), $L\downarrow$ is the descending atmospheric radiance ($W/m^{-2}/sr^{-1}/\mu m^{-1}$), τ is the atmospheric transmissivity, and $L\uparrow$ is the ascending atmospheric radiance ($W/m^{-2}/sr^{-1}/\mu m^{-1}$).

Parameters atmospheric transmissivity and ascending and descending radiance are not present in the metadata of satellite products. These parameters were obtained with the Atmospheric Correction Parameter Calculator tool available online (*Barsi et al.,* 2003). In the calculator data on temperature, altitude, atmospheric pressure, and relative humidity can be introduced. These data were acquired from the National Climatic Data Center of NOAA, specifically from the Vidrasău (Vidrátszeg) weather station (15 km from Marosvásárhely). With this equation, the corrected soil radiance has been obtained, a radiance in which atmospheric effects have been limited.

3.2.3. Obtaining LST from radiance

Thermal infrared bands are transformed into brightness temperature values by the Planck's law inversion equation (*Riaño et al.,* 2000; *Chander et al.,* 2009):

$$B_T = \frac{K_2}{\ln\left(\frac{K_1}{L}+1\right)}, \tag{10}$$

where K_1 (in $W/m^{-2}/sr^{-1}/\mu m^{-1}$) and K_2 (in degrees K) are the calibration constants according to the Landsat thermal band configuration, and L is the spectral radiance ($W/m^{-2}/sr^{-1}/\mu m^{-1}$) calculated previously.

Therefore, the surface temperature (LST) is obtained with the following equation (*Avdan* and *Jovanovska Kaplan,* 2016):

$$S_T = LST = \frac{B_T}{1+\left(\lambda*\frac{B_T}{\rho}\right)\ln(\varepsilon)}, \tag{11}$$

where B_T is the brightness temperature, λ is the wavelength of the radiance emitted in each band. $\rho = h*c/\sigma = 14380$ mK, σ is the Boltzmann constant ($1.38*10^{-23}$ J/K), h is the Planck constant ($6.26*10^{-34}$ Js), and c is the speed of light ($2.998*10^{8}$ m/s). ε is the emissivity of the surface.

From this result 273.15 is subtracted to obtain the LST values in degrees Celsius.

3.3. Comparison of results

An average of the previous years to 2020 was calculated with the LST results of MODIS and Landsat. This result is a mean raster that was compared with the LST raster of 2020.

3.3.1. Dependent t-test for samples

To determine if the LST difference between the mean of 2000–2019 and 2020 whether or not is statistically significant, a t-test of two dependent samples has been performed. The t-test of dependent samples has been chosen because we are measuring the same territory before and after an intervention, that is, the application of anti-COVID measures. Therefore, the factors that make the difference are the time and anti-COVID measures. The t-test was carried out in 7 steps. (1) Definition of the null hypothesis and alternative hypothesis: H_0; μbefore = μafter, H_1; μbefore ≠ μafter. (2) Alpha statement: α = 0.05. (3) Calculation of the degree of freedom: df = N-1. (4) Statement of the order of decision, based on the Student's t distribution t-test table. (5) Calculation of the statistical value of t. (6) Declaration of results. (7) Statement of conclusion. The t-statistic equation is as follows (*Brown* and *Melamed,* 2012):

$$t = \frac{\bar{X}_D}{s_D/\sqrt{n}}, \tag{12}$$

where

$$\bar{X}_D = \frac{(x_i + \cdots + x_n)}{n}, \tag{13}$$

$$s_D = \sqrt{\frac{\sum x^2 - \frac{(\Sigma x)^2}{n}}{n-1}}, \tag{14}$$

where *t* is the dependent test statistic, $\bar{x}_D$ is the mean difference, s_D is the standard deviation of the difference and *n* is the sample size.

The two samples were obtained with the help of Raster Pixels to Points QGIS tool. Then the attribute tables were moved to Excel.

Another paired samples t-test was performed using SPSS for the areas where LST decrease was identified. A mean comparison was made to find out if statistically there is a difference between the mean LST of the areas identified with LST decrease in the lockdown period of 2020 and the mean LST before 2020 (individual available LST data between 2003–2018) in the same period (March 16 -May 14).

3.4. Hotspot-coldspot analysis with Getis-Ord Gi statistic*

The hotspot-coldspot analysis with Getis-Ord Gi* statistic was performed to identify and describe the phenomenon of clustering in the study area of the high (hotspot) and low (coldspot) LST values (*Tran et al.,* 2017; *Ord* and *Getis,* 1995). A single high or low LST value cannot be considered as a cluster. To be

considered as a hotspot or coldspot, a high or low value has to be surrounded by other high or low values. The result of the Getis-Ord Gi* statistic is a z-score. The z-score shows the intensity of clustering; a positive high z-score shows that high values are forming clusters (a hotspot), while a negative high z-score shows that low values are forming clusters (a coldspot). Thus, with the Getis-Ord Gi* statistic, we can better understand the dimensional and spatial changes of LST within the study area. This study has focused especially on the significant change in coldspots. The difference between the average LST of the previous years and 2020 LST shows specific areas in which the temperature has decreased in 2020 concerning to the past. Coldspots with more than 95% confidence level were taken into account. The Getis-Ord Gi* statistic is presented in detail on the ESRI website (*ESRI,* 2016). In this study, the calculation of Getis-Ord Gi* was done with the QGIS Hotspot Analysis plugin. The hotspot-coldspot analysis was carried out in 4 steps: (1) extracting pixel values to points, (2) creating a vector grid layer, (3) counting pixels in polygons with the weight field of the LST value, (4) execution of the hotspot-coldspot local Getis-Ord Gi* analysis.

Other authors have studied LST in urban areas using different urban impact indices such as UTFI (Urban Thermal Field Variance Index) or EEI (Ecological Evaluation Indices) (*Guha et al.,* 2017*,* 2018; *Grover* and *Singh,* 2015; *Jiménez-Muñoz et al.,* 2010).

The average LST values in urban areas were calculated using the QGIS Raster Layer Zonal Statistics tool.

4. Results and discussion

Owing to anthropogenic practices such as land-use change, urban expansion, urban population growth, LST is likely to increase in urban areas (*Singh et al.,* 2017; *Walawender et al.,* 2014; *Zhan et al.,* 2015). However, recent studies have shown that LST can be changed abruptly in urban areas despite urban expansion and population growth; it can decrease with the implementation of measures of suppression of the urban anthropogenic heat, for example the measures of anti-COVID lockdown. This indicates that there is a significant influence of anthropogenic activities on LST regulation (*Li et al.,* 2014; *Lau et al.,* 2020).

Land cover categories can also be distinguished based on their behavior to temperature changes. As they can hold water for the evaporative cooling process, forests and water bodies appear to have comparatively lower LST than urban areas. These land covers (forests and water bodies) increase the flow of latent heat and prevent the transfer of sensitive heat. Dry urban areas, by comparison, magnify responsive heat transfer and impede latent heat flow (*Shahmohamadi et al.,* 2011). Due to their ability to control heat, water bodies tend to have steady temperatures by using the convection mechanism in all segments of the water body (*Jensen,* 2014). *Shahmohamadi et al.* (2011) explain that built-up areas tend

to have higher temperatures than their natural environment around them; this is attributable to land use characteristics and anthropogenic activities.

Built-up areas are consisting of impermeable surfaces and objects, which may lead to an increase in LST due to the lower amount of moisture available to evaporate, according to *Gartland* (2012) (see more: *Matthews,* 2012). Moreover, dark materials restrict incoming short-wave radiation from the Sun within the urban area, and at the same time, buildings can almost completely reduce wind speed. As a consequence, a low wind speed appears to decrease evaporative cooling (*Lee,* 1984). In addition, some authors add that during winter and by the presence of atmospheric pollutants, the impact of anthropogenic activities emitting heat may become more relevant (*Nagy et al.,* 2020; *Offerle et al.,* 2006).

We can conclude from previous studies that relatively higher temperatures in urban areas are influenced not only by the land cover but also by human activities.

4.1. Paired sample t-test result

The Dependent t-test with two dependent samples (Landsat LST 2020 and Landsat LST 2003 – 2018) showed that our H1 hypothesis is true ($\mu before \neq \mu after$), that is, the time and/or anti-COVID measures taken in 2020 have a statistically significant effect on the change in LST, $t = -432.7$, critical value = 1.96, $p < 0.05$.

4.2. Comparison of the average LST in the lockdown period (March 16 –May 14) of 2020 with the average for the years 2000–2019 in the same period

The average LST for the period March 16–May 14, 2020, which corresponds to the confinement period, has been compared with the average for the years 2000–2019 for the same period. In *Fig. 2*, which presents the MODIS data, we can see that during 2000 and 2019, high values of LST are found in urban areas. The situation in 2020 seems to follow the same trend. The difference map highlights the areas that show the positive and negative change. The urban environment, which stands out in the descent of the LST is the Tudor (Sásvári) district, a neighborhood characterized by the density of tall buildings and few vegetation. This neighborhood is the most crowded in the city with a significant impact on traffic and population density. For this reason, it has the greatest descent change (negative change) of LST.

Because Landsat has a higher spatial resolution, we can see in more detail the areas with high and low temperatures and the areas that have changed (*Fig. 3*).

Landsat results corroborate the MODIS results: the distribution of high and low values is different in 2020 than the long average of data existing between 2003–2018.

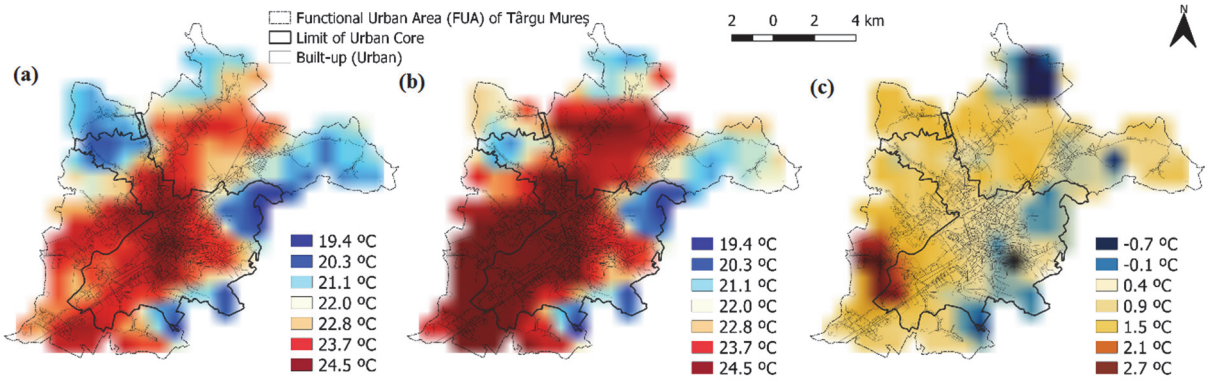

Fig. 2. MODIS LST (a) between 2000–2019, (b) in 2020, and (c) the difference between them.

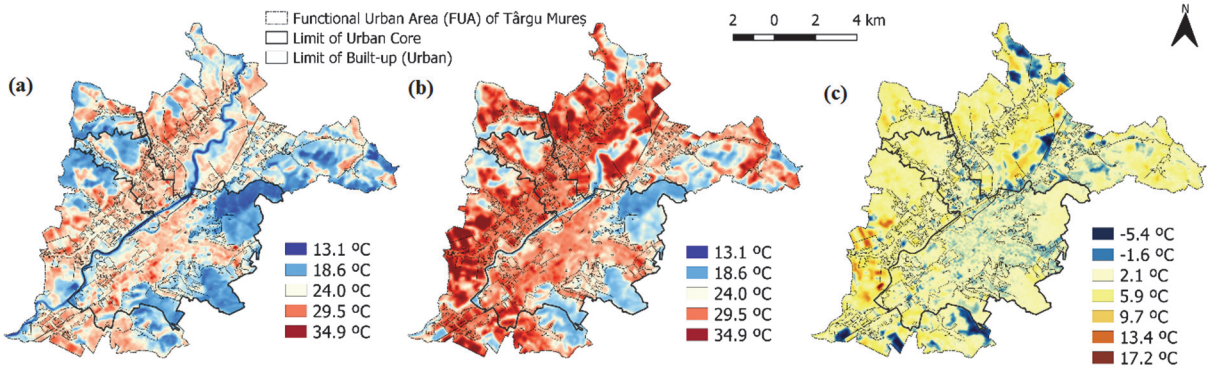

Fig. 3. Landsat LST (a) between 2003–2018, (b) in 2020, and (c) the difference between them.

Although we have higher values in 2020 in urban areas, their concentration has been reduced in some areas. However, in 2020 we can still observe existing heat islands (e.g., areas of the Azomureș industrial estate). The Tudor district also stands out in the difference raster.

Both MODIS and Landsat data show an increase in LST, in general in built-up areas. The trends in LST described below are also including the study period in 2020. The average value observed in 2000–2019 for MODIS and in 2003–2018 for Landsat images, respectively, has been subtracted from the value observed in 2020. MODIS shows an increase of +0.78 °C (average for the years 2000–2019: 23.3 °C and average of 2020: 24.1 °C), while Landsat shows an increase of +2.36 °C (average for the years 2003-2018: 24.7 °C and average of 2020: 27.0 °C).

The range of the maximum and minimum values is also different between MODIS and Landsat (MODIS: 0.79 °C, Landsat: -2.97 °C). We have a negative difference range in the case of Landsat (2003-2019 average range and 2020 range), because the range between the minimum and maximum values in the year 2020 was almost 3 °C lower (17.1 °C) than during the years 2003–2018 (20.0 °C). In the case of MODIS, this average range difference between 2000–2019 and

2020 range is not even 1 ° Celsius (the average range 2000–2019 is 4.0 °C and the 2020 range is 4.8 °C) and, on the contrary, here we have a larger range in 2020 (4.8 °C) than during 2000-2019 (4.0 °C), which gives a positive range difference. Thus, Landsat shows a much higher range than MODIS; that is, the minimum and maximum values are quite different between 2003–2018 and 2020. This is reflected in the standard deviations as well (MODIS LST 2020: σ = 1.04, MODIS LST 2000– 2019: σ = 0.92, Landsat 2020: σ = 1.71, Landsat 2003–2018: σ = 1.62). The difference in standard deviations between MODIS and Landsat shows that MODIS σ = 0.12, Landsat σ = 0.08. These differences between MODIS and Landsat are relevant to the LST trend, because they show how spatial resolution and acquisition methods of satellite images can influence the LST values obtained. Due to its higher spatial resolution, Landsat can better detect objects with higher or lower LST emissions.

Differences between MODIS and Landsat are due to the different spatial resolution of the two sensors (Landsat LST offers more details about the territory and the objects) and the different modes of capturing the TIR and obtaining the LST.

Fig. 4 shows the trend of LST between the years 2000–2020 with MODIS data in the built-up area. A downward trend can be observed between 2000–2005, however, after 2005, this becomes an upward trend of LST.

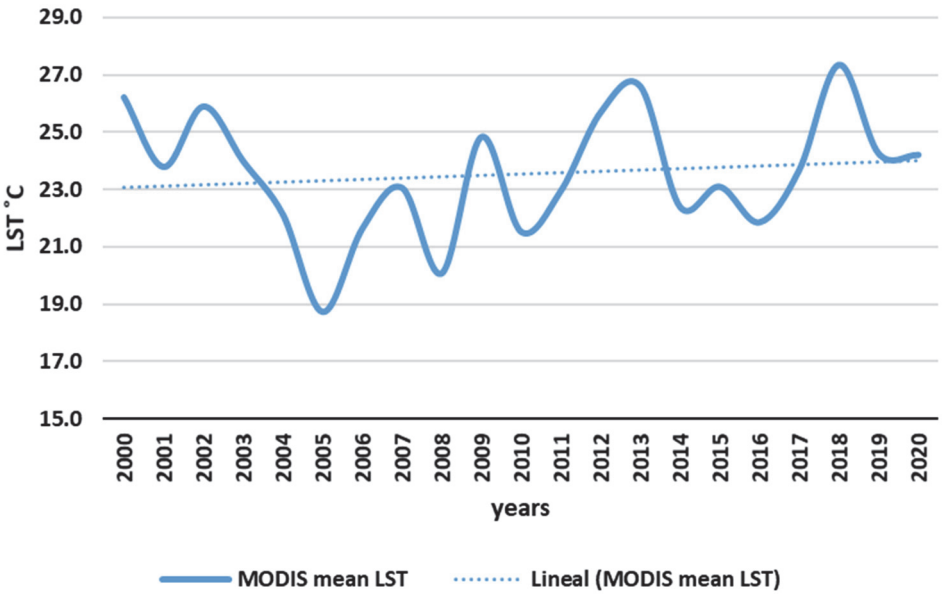

Fig. 4. MODIS mean LST evolution in the general built-up land cover (time period: March 16–May 14).

The timeseries analysis also indicates an increase of +0.72 °C in the case of MODIS data. However, if we take only the last three years (2019, 2018, 2017), we are talking about a decrease of -1 °C in urban areas. This points out that to have a broad and detailed view of how much and how LST has changed with the

implementation of anti-COVID measures, it is not enough to take into consideration only the last few pairs of years, as some studies have done so far (*Maithani et al.,* 2020). At the global level, climate change also affects large and medium-sized cities, so more years should be taken when comparing with the 2020 situation. Time-series analysis shows that LST in urban areas tends to increase since 2000, although in the case of Marosvásárhely, there has been no significant urban expansion since 2000.

The increase in temperature in the urban area is due to climate change that causes even warmer cities. If we analyze the LST data of Landsat (only the data that we have), we see that we have an increase of +2.5 °C in the built areas in general. The evolution of the average LST in the built-up area with Landsat data shows two peaks throughout the images available between 2003–2020 in the month of April: in 2007 (27.3 °C) and 2018 (32.6 °C) (*Fig. 5*). An upward LST trend is also observed.

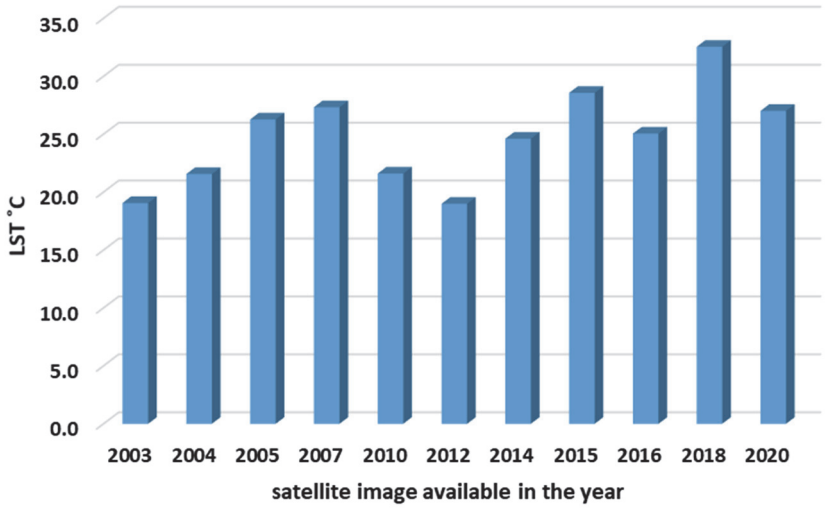

Fig. 5. Landsat mean LST evolution in the general built-up (urban) land cover over available Landsat images.

The difference between the trend detailed above first and the trend of timeseries analysis is that the former was calculated by adding the LST raster layers of the years prior to 2020 and dividing by the total number of years (20); thus comparing the resulting average raster layer of the years 2000–2019 with the raster layer of 2020 using the zonal statistics method for the urban area. The second trend analysis was also calculated with the zonal statistics method. However, this time we calculated the average value of LST for each year separately in the urban area. These observations were placed in a table, thus achieving the graphical representation of the trend (*Figs. 4* and *5*).

4.3. LST anomaly analysis

Similarly to the LST temperature calculation, the LST anomaly with MODIS data was calculated for the study period between March 16 and May 14 for the years 2000–2020. These LST anomaly results for the different years are raster layers representing the LST anomaly within March 16 – May 14 in 2000–2020. For the years 2000–2019, an average resulting in a single LST anomaly average raster has been calculated. The 2020 anomaly is not included in this average, because the mean raster of 2000–2019 is subtracted from the 2020 raster, thus obtaining the LST anomaly difference.

We calculated the monthly anomaly as the difference between the monthly climatology minus the average of months within the study period, i.e., March-May. Then the rasters between 2000–2019 are added, and a long average comparing with the 2020 raster is calculated.

Fig. 7 represents the average monthly LST anomaly in the period March 16 - May 19, 2000–2019 and in 2020. It can be observed that in 2020, the concentration of high values of positive thermal anomaly is still present in urban areas. This also shows that the spatial distribution of high and low values is different in 2020 than in previous years.

The LST anomaly trend in the built-up area reached the minimum point in 2005, when the average anomaly in the built-up was the most lower (+0.2 °C). After 2005 the variation persists, however, an upward trend is observed over time, touching the maximum value observed during 2000–2020 in 2018 (+6.4 °C) (*Fig. 6*).

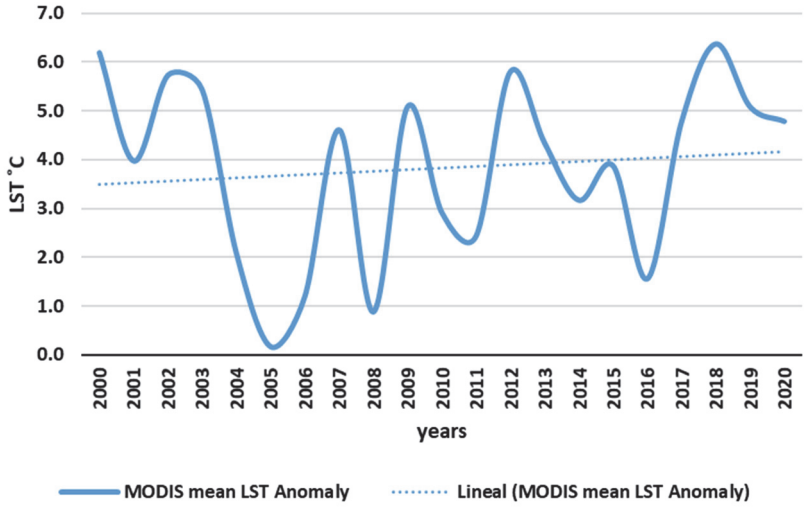

Fig. 6. MODIS mean LST anomaly in the general built-up (urban) land cover (time period: March 16–May 14).

The timeseries analysis of the anomaly shows an increase of positive LST anomaly of +1 °C by 2020 for the long average of the years 2000–2019. The anomaly trend analysis does not include the year 2020, because the average of 2000–2019 has

compared with the average anomaly observed in 2020. Again, if we look only at the last three years, it shows an anomaly decrease of -0.6 °C (*Fig. 6*).

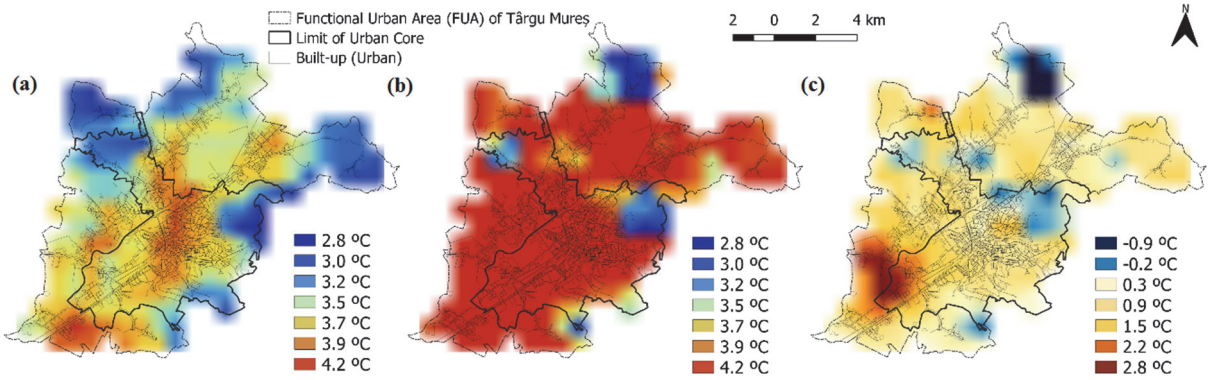

Fig. 7. LST anomaly (a) between 2000–2019, (b) in 2020, and (c) the difference between them.

4.4. . Change in the categories of built-up areas

Urban categories correspond to the land cover classification of the Urban Atlas (Copernicus Programme, Copernicus Land Monitoring Service) (*Fig. 8*). This methodology classifies urban areas into different categories according to characteristics and land use.

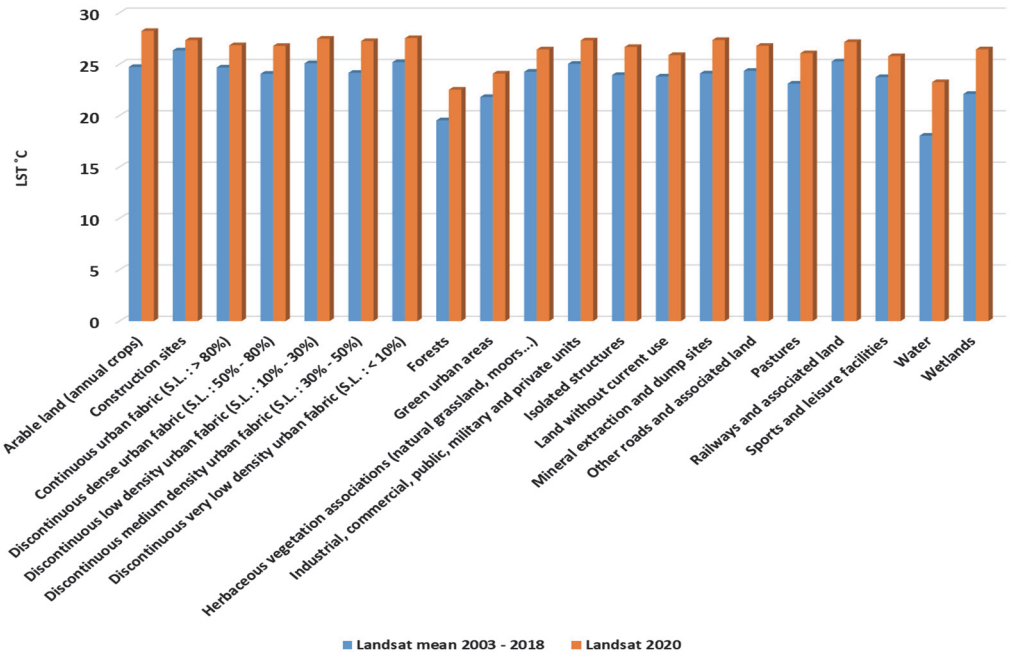

Fig. 8. Landsat LST in different land cover categories. Comparison between the mean LST of available images and 2020 (time period: March 16–May 14).

The LST analysis of urban area categories also shows an increase of LST in 2020 for all urban categories compared to the average of previous years.

The urban type that experienced the greatest increase is the "Discontinuous medium density urban fabric (S.L.: 30–50%)" (+3.1 °C). Other categories are similar in terms of the increase in temperature (about +2.4 °C).

Based on the land use data from the Urban Atlas, it is also purposeful to see what differences exist between the different land categories present in the functional urban area (FUA) of Târgu Mureș concerning the average before 2020 and the situation in 2020 (*Fig. 8*). The largest increase in LST occurs in the categories "Water" (+5.2 °C) and "Wetlands" (+4.3 °C). This change also refers to the fact that thermal anomaly persists more in water bodies. The reclassification of all these land-use types into four representative categories of the territory ("Built-up (Urban)", "Vegetation", "Water", "Bare soil") also shows that water bodies are more likely to register a positive change, an LST increase (+5.1 °C) (*Fig. 9*). On the contrary, the smallest increment in LST is recorded in the category "Bare soil" (+2.1 °C) which land type is more likely to catch and lose temperature more quickly due to the lack of vegetation. The "Built-up (Urban)" category also behaves similarly (+2.4 °C) because of the nature of the building and street materials (*Fig. 9*).

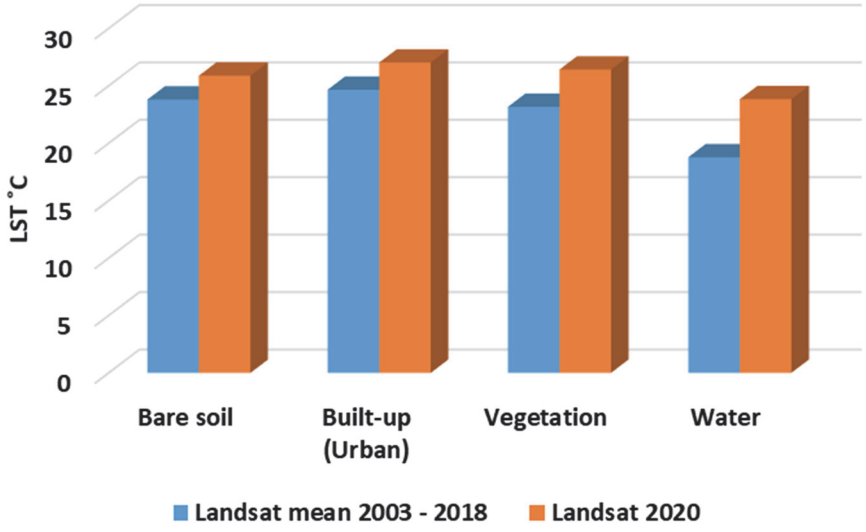

Fig. 9. Landsat LST in reclassified land cover categories. Comparison between the mean LST of available images and 2020 (time period: March 16 - May 14).

4.5. Coldspot analysis and areas with LST drop

Despite the general increase of LST in the built-up areas, with the hotspot-coldspot analysis of Getis-Ord Gi* is possible to identify areas with a decrease in LST in 2020 concerning the average of the previous years (*Fig. 11(a)*).

Looking at these coldspots on a Google Satellite Hybrid map, it was observed that they largely correspond to factory areas, public transport centers,

shopping malls, and industrial polygons (*Fig. 11*). The Mureșeni (Meggyesfalvi)–Orașul de Jos (Bega) and Tudor (Sásvári) dictricts stand out in the number of cases. These districts are located on a west-east axis, which is the direction of the western winds. The Azomureș industrial area of national interest is located in the western part of the city. It can have an impact on the fact that these districts have significant temperature drops. On the other hand, open fields and the river Mureș show significant hotspots in terms of the difference between 2020 and the long average of the previous years.

In the case of the River Mureș, this is due to climate change. It has to be connected to the sensitivity of rivers to climate change (*Nijssen et al.*, 2001) because if a positive temperature anomaly persists in a river basin, waterbodies can store heat for longer. Other parts can also experience climate change. However, the temporal variability of the LST due to weather conditions increases, because bodies on the Earth's surface get warmer and cooler faster, and most of them are not able to store heat any longer like waterbodies.

If we focus on the map presented in *Fig. 10(b)* showing hot and cold spots in 2020, we can see that there are few clusters (hole phenomenon) within the city compared to 2013-2018 (*Fig. 10(a)*). The Azomureș chemical industrial area and other areas related to the industry also operated between March 16 –May 14, 2020, and these hotspots remained unchanged in 2020. *Fig. 11(a)* shows the difference between the LST raster of 2020 and the LST raster of 2003–2018.

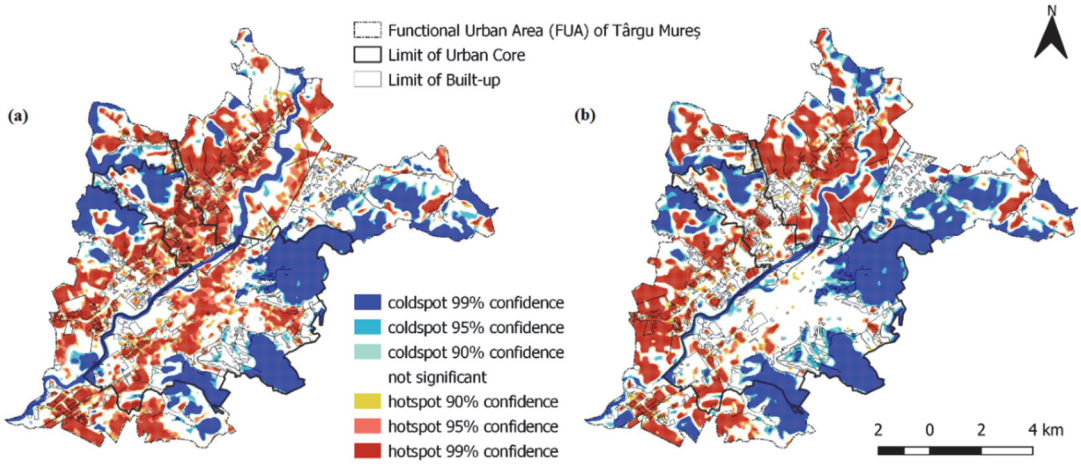

Fig. 10. Significant LST hotspots and coldspots (a) between 2003–2018 and (b) in 2020.

The total area of the built-up (urban) area is 33.84 km^2. The size of the area that has experienced a decrease in surface temperature is 0.24 km^2, which is equivalent to only 1% of the total built-up area; these are mostly areas of factories, industrial polygons, shopping centers, and public transport centers (*Table 2*). However, if we take the entire area of the significant coldspot change (confidence

level of 99%) within the built-up area (*Fig. 11(b)*), this percentage is 11% (3.71 km^2) of the total built-up area. The fifth column of *Table 2* indicates the minimum LST temperature of the area of that coldspot. The average of the minimum values of these 46 cases is -0.61 °C. However, there are cases with LST loss below -1 °C. In the first column (N), the number marked with the upper index ** represents cases with LST decrease below -2 °C. The number marked with the upper index *, on the other hand, indicates cases with an LST drop below -1 °C.

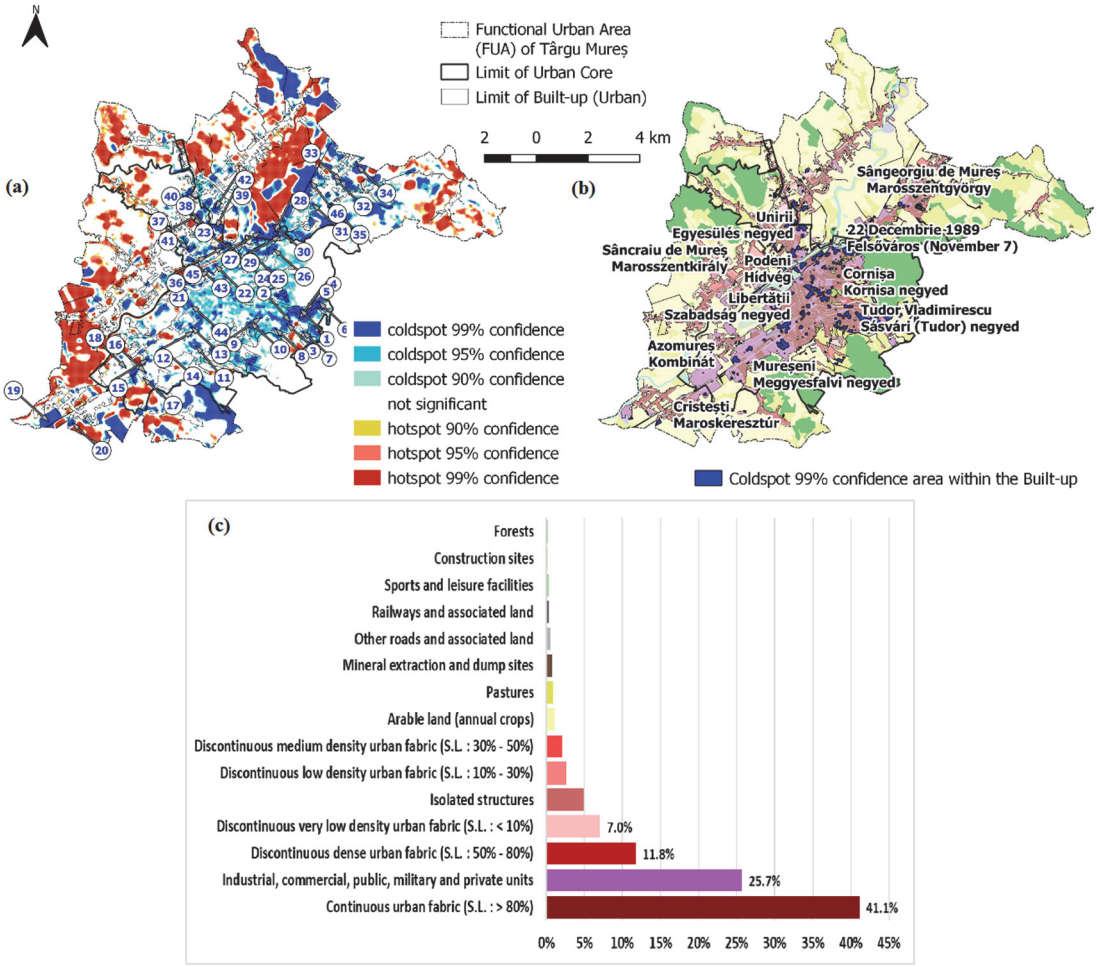

Fig. 11. (a) LST change hotspots and coldspots, (b) significant coldspots within the built-up areas (see *Table 2*), and (c) relative frequency of land cover types within the changing coldspots (confidence level of 99%) in the urban area.

The relative frequency of land cover types within significant coldspots (confidence level 99%) in the built area shows that 41.1% of the total area of cold spots corresponds to the category "Continuous urban fabric (S.L. > 80%)" (*Fig. 11(c)*). Another 25.7% of the coldspot areas corresponds to the category "Industrial, commercial, public, military and private units" and, also, 11.8% belong to the "Discontinuous dense urban fabric (S.L. 50%–80%)" category.

Table 2. Decreased areas in LST; category type, name of location, and the minimum LST value of decrease. The number marked in the first column (N) with the upper index * indicates cases with LST decrease below -1 °C, while ** indicates the cases with an LST drop below -2 °C (Fig. 11)

N	Type	District	Constituent building name	Min LST decrease (°C)
1**	Industrial, Commercial	Tudor (Sásvári)	SC Sumel Maşini de Calcul SA; ROTECOM S.R.L.; Meesenburg România - sediul central; Coralia Com Srl Depozit Tg. Mures; SELDOR S.R.L; Sameday Curier Târgu Mureș	**-2.58**
2	Commercial, Industrial, Service	Tudor (Sásvári)	U-Rent - Închirieri Remorci; X-Tend MOB; ITP Nova Service; SC PARTNER ALU PLAST SRL; Gold Gym Fitness & Aerobics	-0.69
3	Services	Tudor (Sásvári)	ELIT; Merkúr	-0.00021
4	Residential	Tudor (Sásvári)	Houses	-0.22
5	Commercial	Tudor (Sásvári)	Ropharma	-0.26
6	Residential	Tudor (Sásvári)	Mansions	-0.37
7	Services, Commercial	Tudor (Sásvári)	Auchan	-0.44
8	Industrial, Services	Tudor (Sásvári)	Euro Gas Systems: Vessels & CNC; CarXpert Mures | Service Auto & Tractări	-0.34
9	Services, Commercial	Tudor (Sásvári)	Area of Profi Moldovei	-0.03
10	Transportation Services	Tudor (Sásvári)	MOL gas station; Crossroad Bulevardul Pandurilor - Strada Secerei	-0.10
11*	Industrial, Transportation	Orașul de Jos (Bega)	Industrial area of Orașul de Jos quarter: TMF Manufacturing Solutions SRL; Roseco SRL; Novoparts SRL; PLASTERM S.A.; Siletina SC Transport Local SA; Autogara Voiajor Marosvásárhely; Surtec; Bioeel; FrieslandCampina	**-1.33**
12	Residential	Orașul de Jos (Bega)	Strada Făgărașului	-0.0001
13	Commercial, Transportation	Orașul de Jos (Bega)	Near the CFR locomotive depot	-0.10
14	Commercial	Mureșeni (Meggyesfalvi)	Commercial Area: Natürlich - mobilier und decoratiuni, Tg.Mures; Melinda Instal; SC Vargas Seminee SRL; Total Sport Distribution SRL; Kober SRL - Mureș	-0.82
15	Industrial, Commercial	Mureșeni (Meggyesfalvi)	Industrial Area: Mobex polygon area; Panservice; Urgent Cargus	-0.90
16	Services	Mureșeni (Meggyesfalvi)	Recreation Area: Hotel Imperial Inn; Imperial Spa. Service Area: Turbo Logic; TEKAROM SRL; Professional Recycle	-0.98
17	Commercial, Services	Mureșeni (Meggyesfalvi)	Metro	-0.25
18	Industrial	Mureșeni (Meggyesfalvi) - Azomureș	Azomureș	-0.45
19*	Services: Water treatment plant	Cristești (Maroskeresztúr)	Aquaserv	**-1.84**
20	Services, Commercial	Cristești (Maroskeresztúr)	Leco AGRO; SC VERAL COM SRL	-0.16
21	Services	Centru (Főtér)	Multipurpose Hall (Sala Polivalentă)	-0.05
22*	Industrial	Centru (Főtér)	Electromureș S.A.	**-1.75**

Table 2. Continued

N	Type	District	Constituent building name	Min LST decrease (°C)
23	Services	Aleea Carpați (Kárpátok-sétány)	Area near Pensiunea Mureșul	-0.32
24	Residential	Aleea Carpați (Kárpátok-sétány)	"Area of the apartment"	-0.02
25	Industrial	22 Decembrie (Felsőváros)	Furniture Mobex factory area	-0.72
26	Services	22 Decembrie (Felsőváros)	Area of Emergency County Hospital Marosvásárhely	-0.55
27*	Residential	Sângeorgiu de Mureș	New houses - Strada Petőfi Sándor utca	**-1.17**
28	Residential	Sângeorgiu de Mureș	Houses - Strada Mihai Eminescu utca	-0.14
29	Commercial	22 Decembrie (Felsőváros)	Nakita Prod Comimpex S.R.L.; Accesorii Ancorare Marfă	-0.08
30	Industrial	Sângeorgiu de Mureș (Marosszentgyörgy)	Manufacture complex - Strada Sudului	-0.80
31	Industrial, Commercial	Sângeorgiu de Mureș (Marosszentgyörgy)	Buildings	-0.15
32*	Industrial, Services	Sângeorgiu de Mureș (Marosszentgyörgy)	SC Gastrometal SRL; AD GARAGE GOLDFIT SERVICE; A.C.R Sângeorgiu de Mureș	**-1.27**
33	Services	Sângeorgiu de Mureș (Marosszentgyörgy)	TinyHome - Închirieri autorulote	-0.30
34	Residential	Sângeorgiu de Mureș (Marosszentgyörgy)	Houses	-0.17
35	Residential	Sângeorgiu de Mureș (Marosszentgyörgy)	Houses	-0.63
36	Transportation, Industrial	Podeni (Hídvég)	Hídvég Crossroad; Romcab S.A.	-0.20
37	Residential	Podeni (Hídvég)	Houses	-0.31
38*	Industrial	Unirii (Egyesülés)	Strada Apaductului	**-1.05**
39**	Industrial	Unirii (Egyesülés)	Foto	**-2.80**
40	Residential	Unirii (Egyesülés)	Houses	-0.09
41	Residential	Unirii (Egyesülés)	Unirii Park Residence	-0.17
42*	Industrial	Unirii (Egyesülés)	AUNDE C&S AUTOMOTIVE S.R.L.	**-1.16**
43	Transportation	Sâncraiu de Mureș (Marosszentkirály)	Road	-0.10
44	Commercial	Libertății (Szabadság)	S.C. ADIMAG COMIMPEX S.R.L.	-0.08
45	Commercial	Unirii (Egyesülés)	Palas com	-0.25
46*	Residential	Sângeorgiu de Mureș (Marosszentgyörgy)	Houses	**-1.78**

4.6. Paired sample t-test for areas identified with LST decrease

To be able to affirm that the decrease of the LST in these 46 cases can be explained with the application of the anti-COVID measures, it is examined statistically whether there is a difference between the mean LST of the areas identified with LST decrease in the lockdown period of 2020 and the mean LST before 2020 (i.e., 2003–2018) in the same period (March 16 –May 14) (*Table 3*). For this purpose, we use the available Landsat data.

The null hypothesis (H_0) is that the mean of the *before LST* is equal to the mean of the *after LST* measurement (μbefore = μafter). In other words, there is no difference between LST measured before 2020 with no anti-COVID measures applied, and LST measured in 2020 with anti-COVID measures applied.

The alternative hypothesis (H_1) is that the mean of the *before LST* is not equal to the mean of the *after LST* measurement (μbefore ≠ μafter). In other words, there is a difference between LST before 2020 with no anti-COVID measures applied, and LST in 2020 with anti-COVID measures applied.

We test this with an alpha value equal to 0.05, which is equal to 95% confidence level.

In the 46 cases, the mean LST of 2020 was compared with the mean LST of previous years. The comparative results of the averages show that in all pairs, the t statistical value is less or greater than the critical value (2.000), which corresponds to the degree of freedom (45). Likewise, the p-value in all pairs is less than 0.05 (*Table 3*). Therefore, we can conclude that there is a statistically significant difference in the average LST before and after anti-COVID measures in the areas identified with LST decrease.

Table 3. Paired samples t-test comparing the average difference of Landsat 2020 mean LST and previous years mean LST in the areas identified with LST decrease. Column t shows the t-test values, df is the degree of freedom, and Sig. (2-tailed) shows the significance of p value for each pair (this test is done with an α = 0.05)

Paired samples t-test									
		Paired differences							
					95% confidence interval of the difference				
Landsat mean LST		Mean	Std. deviation	Std. error mean	Lower	Upper	t	df	Sig. (2-tailed)
Pair 1	2020 - 2018	-8.38965	2.35986	0.34794	-9.09045	-7.68886	-24.112	45	0.000
Pair 2	2020 - 2016	-1.13292	2.37514	0.35019	-1.83824	-0.42759	-3.235	45	0.002
Pair 3	2020 - 2015	-3.24816	1.99564	0.29424	-3.84079	-2.65553	-11.039	45	0.000
Pair 4	2020 - 2014	1.30848	1.21359	0.17893	0.94809	1.66887	7.313	45	0.000
Pair 5	2020 - 2012	4.56721	1.64654	0.24277	4.07825	5.05617	18.813	45	0.000
Pair 6	2020 - 2010	3.53593	1.29481	0.19091	3.15142	3.92045	18.521	45	0.000
Pair 7	2020 - 2007	-3.93599	1.28956	0.19013	-4.31894	-3.55304	-20.701	45	0.000
Pair 8	2020 - 2005	-2.46037	1.94611	0.28694	-3.03830	-1.88245	-8.575	45	0.000
Pair 9	2020 - 2004	1.81966	1.83836	0.27105	1.27374	2.36559	6.713	45	0.000
Pair 10	2020 - 2003	4.68105	1.87976	0.27716	4.12283	5.23927	16.890	45	0.000
Pair 11	2020 - Mean years 2003-2018	-0.32548	0.30425	0.04486	-0.41583	-0.23512	-7.255	45	0.000

5. Conclusions

In Marosvásárhely city, the land surface temperature (LST), despite the anti-COVID measures applied between March 16 -May 14 corresponding to the lockdown period, was increased by 1–2 °C in general in urban areas compared to the previous years of 2000-2019. It can be explained by the insufficiency and weakness of the anti-COVID measures adopted. Anti-COVID measures could not reverse the process of increasing LST and positive LST anomaly throughout urban areas.

However, anti-COVID measures have not been completely ineffective. 46 cases of coldspots within urban areas show a decline in LST due to the 2020 health emergency. The vast majority of these coldspots are areas that perform economic and transport activity, so, logically, the anti-COVID measures have mainly affected these areas.

Coldspots are interpreted as a negative LST change and not as a downward trend. The 46 cases of coldspots are resulted from the difference between the 2020 raster and the average raster of 2003–2018. (These Landsat data do not include every year between 2000–2019, because no useful satellite image had found in these years just after applying the anti-COVID measures in the study period). This difference raster shows areas where compared to previous years, LST has decreased or increased in 2020. This raster layerwas used to identify statistically significant coldspots.

Consequently, according to the difference between the 2003–2018 average and 2020, the 46 identified cases within the urban land class are specific areas that have transformed into coldspots.

The percentage of the total size of the area that has shown a negative change, that is, it has become colder in the lockdown period of 2020 than during the same period of the previous years, is about 1% (0.25 km^2) of the total built-up area (33.8 km^2). However, if we take the significant coldspots of change (confidence level of 99%) within the built-up area as a measure, this percentage goes up to 11% (3.71 km^2). The most frequent built-up area type within the significant coldspots (confidence level of 99%) is the "Continuous urban fabric (S.L. > 80%)" (41.1%), followed by the categories "Industrial, commercial, public, military and private units" (25.7%), and "Discontinuous dense urban fabric (S.L. 50%–80%)" (11.8%), which are typically urban categories.

Paired samples t-test performed for the areas identified with LST decrease shows that there is a statistically significant difference ($p < 0.05$) of the average LST between the years before 2020 and 2020, which may indicate evidence of the implication of anti-COVID measures to the decline of LST in these areas carrying out economic and transport activities. This shows that in a medium-sized city such as Marosvásárhely, anti-COVID measures have caused a decrease in land surface temperature in specific areas (*Fig. 11, Tables 2* and *3*).

The MODIS LST data are satisfactory for identifying general trends and patterns at global or moderate geographical scale. However, for a hotspot-coldspot analysis of the urban heat islands, it is more appropriate to use Landsat satellite data.

Limitations of the study: To show irrefutably that the anti-COVID measures had a significant effect on the decline of LST, more or all medium-sized cities would have to be analyzed at a country level or the European continental level. The nature and effectiveness of the measures should be taken also into account in each country or region. Therefore, other studies should compare more cities in the same administration region or the same country.

Acknowledgment: The authors wish to express appreciation to the free software developers of QGIS and Google Earth Engine.

References

Agrawal, S., Bhandari, S., Bhattacharjee, A., Deo, A., Dixit, N. M., Harsha, P., . . ., and *Yasodharan, S.*, 2020: City-Scale Agent-Based Simulators for the Study of Non-pharmaceutical Interventions in the Context of the COVID-19 Epidemic: IISc-TIFR COVID-19 City-Scale Simulation Team. *J. Indian Inst. Sci. 100*(4), 809–847. https://doi.org/10.1007/s41745-020-00211-3

Avdan, U. and *Jovanovska Kaplan, G.*, 2016: Algorithm for Automated Mapping of Land Surface Temperature Using LANDSAT 8 Satellite Data. *J. Sensors, 2016*(2), 1–8. https://doi.org/10.1155/2016/1480307

Awasthi, A., Sharma, A., Kaur, P., Gugamsetty, B., and *Kumar, A.,* 2021: Statistical interpretation of environmental influencing parameters on COVID-19 during the lockdown in Delhi, India. *Environment, Development and Sustainability 23,* 8147–8160. https://doi.org/10.1007/s10668-020-01000-9

Barsi, J. A., Barker, J. L., and *Schott, J. R.*, 2003: An Atmospheric Correction Parameter Calculator for a single thermal band earth-sensing instrument. *IEEE International Geoscience and Remote Sensing Symposium 2003*, *5*, 3014–3016. Toulouse. https://doi.org/10.1109/IGARSS.2003.1294665

Barsi, J. A., Hook, S. J., Palluconi, F. D., Schott, J. R., and *Raqueno, N. G.*, 2006: Landsat TM and ETM+ thermal band calibration. En J. J. Butler (Ed.), *Earth Observ. Syst.XI*, *6296.* San Diego. doi:10.1117/12.683212. https://doi.org/10.1117/12.683212

Brown, S. and *Melamed, L.*, 2012: T Test, In: Experimental Design and Analysis. SAGE Publications, Inc., 10–12. https://doi.org/10.4135/9781412984218.n3

Buyantuyev, A. and *Wu, J.*, 2010: Urban heat islands and landscape heterogeneity: linking spatiotemporal variations in surface temperatures to land-cover and socioeconomic patterns. *Landscape Ecol 25*, 17–33. https://doi.org/10.1007/s10980-009-9402-4

Ceccato, P., Pietsch, V., Chen, Y.-J., Marconi, B., Balk, C., and *Stevenson, A.,* 2017: JavaScript: Using Google Earth Engine to Analyze Land Surface Temperature by benjamin.j.marconi - issuu. International Research Institute for Climate Society, Earth Institute, Columbia University,. URL https://issuu.com/benjamin.j.marconi/docs/iri_analysis_of_temperature_data.docx (accessed 12.29.20).

Chander, G., Markham, B. L., and *Helder, D. L.*, 2009: Summary of current radiometric calibration coefficients for Landsat MSS, TM, ETM+, and EO-1 ALI sensors. *Remote Sens. Environ. 113*, 893–903. https://doi.org/10.1016/j.rse.2009.01.007

Coll, C., Galve, J. M., Sanchez, J. M., and *Caselles, V.*, 2010: Validation of Landsat-7/ETM+ Thermal-Band Calibration and Atmospheric Correction With Ground-Based Measurements. *IEEE Trans. Geosci. Remote Sens., 48*, 547–555. https://doi.org/10.1109/TGRS.2009.2024934

Dissanayake, D., Morimoto, T., Murayama, Y., and *Ranagalage, M.*, 2019a: Impact of Landscape Structure on the Variation of Land Surface Temperature in Sub-Saharan Region: A Case Study of Addis Ababa using Landsat Data (1986–2016). *Sustainability 11*, 2257. https://doi.org/10.3390/su11082257

Dissanayake, D., Morimoto, T., Murayama, Y., Ranagalage, M., and *Handayani, H. H.*, 2019b: Impact of Urban Surface Characteristics and Socio-Economic Variables on the Spatial Variation of Land Surface Temperature in Lagos City, Nigeria. *Sustainability, 11*(1), 25. https://doi.org/10.3390/su11010025

Donegan, S. J., and *Flynn, L. P.*, 2004: Comparison of the response of the Landsat 7 Enhanced Thematic Mapper Plus and the Earth Observing-1 Advanced Land Imager over active lava flows. *J. Volcanol. Geothermal Res. 135*(1-2), 105–126. https://doi.org/10.1016/j.jvolgeores.2003.12.010

Dousset, B., Luvall, J.C., and *Hulley, G.C.*, 2019: Surface Temperatures in the Urban Environment, In: Taking the Temperature of the Earth (eds. *Hulley, G. C.* and *Ghent, D.*). Elsevier, 203–226. https://doi.org/10.1016/B978-0-12-814458-9.00007-1

Du, C., Ren, H., Qin, Q., Meng, J., and *Zhao, S.*, 2015: A Practical Split-Window Algorithm for Estimating Land Surface Temperature from Landsat 8 Data. *Remote Sens. 7*(1), 647–665. https://doi.org/10.3390/rs70100647

Duan, S.-B., Li, Z.-L., Li, H., Göttsche, F.-M., Wu, H., Zhao, W., . . ., and *Coll, C.*, 2019: Validation of Collection 6 MODIS land surface temperature product using in situ measurements. *Remote Sens. Environ. 225*, 16–29. https://doi.org/10.1016/j.rse.2019.02.020

Eleftheriou, D., Kiachidis, K., Kalmintzis, G., Kalea, A., Bantasis, C., Koumadoraki, P., . . ., and *Gemitzi, A.*, 2018: Determination of annual and seasonal daytime and nighttime trends of MODIS LST over Greece - climate change implications. *Sci. Total Environ. 616–617*, 937–947. https://doi.org/10.1016/j.scitotenv.2017.10.226

ESRI, 2016: How Hot Spot Analysis (Getis-Ord Gi*) works. Retrieved 12 16, 2020, from https://desktop.arcgis.com/en/arcmap/10.3/tools/spatial-statistics-toolbox/h-how-hot-spot-analysis-getis-ord-gi-spatial-stati.htm

Gallo, K. P., McNab, A. L., Karl, T. R., Brown, J. F., Hood, J. J., and *Tarpley, J. D.*, 1993: The Use of NOAA AVHRR Data for Assessment of the Urban Heat Island Effect. *J. Appl. Meteorol. Climatol. 32*(5), 899–908. https://doi.org/10.1175/1520-0450(1993)032<0899:TUONAD>2.0.CO;2

Gartland, L., 2012: Heat Islands: Understanding and mitigating heat in urban areas (1 ed.). London, UK: Routledge. https://doi.org/10.4324/9781849771559

Grover, A. and *Singh, R.B.*, 2015: Analysis of Urban Heat Island (UHI) in Relation to Normalized Difference Vegetation Index (NDVI): A Comparative Study of Delhi and Mumbai. *Environments 2*, 125–138. https://doi.org/10.3390/environments2020125

Guha, S., Govil, H., and *Mukherjee, S.*, 2017: Dynamic analysis and ecological evaluation of urban heat islands in Raipur city, India. *J. Appl. Remote Sens. 11*(3), 036020. https://doi.org/10.1117/1.JRS.11.036020

Guha, S., Govil, H., Dey, A., and *Gill, N.*, 2018: Analytical study of land surface temperature with NDVI and NDBI using Landsat 8 OLI and TIRS data in Florence and Naples city, Italy. *Eur. J. Remote Sens. 51*(1), 667–678. https://doi.org/10.1080/22797254.2018.1474494

Hadibasyir, H. Z., Rijal, S. S., and *Sari, D. R.*, 2020: Comparison of Land Surface Temperature During and Before the Emergence of Covid-19 using Modis Imagery in Wuhan City, China. *Forum Geografi 34*(1), 1–15. https://doi.org/10.23917/forgeo.v34i1.10862

Hulley, G. C., Ghent, D., Göttsche, F. M., Guillevic, P. C., Mildrexler, D. J., and *Coll, C.*, 2019: Land Surface Temperature, In: Taking the Temperature of the Earth (eds. *Hulley, G.C., and Ghent, D.*). Elsevier, 57–127. https://doi.org/10.1016/B978-0-12-814458-9.00003-4

Hulley, G. C., Hughes, C. G., and *Hook, S. J.*, 2012: Quantifying uncertainties in land surface temperature and emissivity retrievals from ASTER and MODIS thermal infrared data. *J. Geophys. Res.: Atmospheres, 117*(D23), 1–18. https://doi.org/10.1029/2012JD018506

Imhoff, M. L., Zhang, P., Wolfe, R. E., and *Bounoua, L.*, 2010: Remote sensing of the urban heat island effect across biomes in the continental USA. *Remote Sens. Environ. 114*(3), 504–513. https://doi.org/10.1016/j.rse.2009.10.008

Institutul Național de Statistică, 2011: Rezultate | Recensamant 2011. *Recensământul populației și al locuințelor*,. URL http://www.recensamantromania.ro/rezultate-2/ (accessed 12.30.20). (In Romaian)

Jensen, J. R., 2014: Remote Sensing of the Environment: An Earth Resource Perspective (2 ed.). Harlow, Essex, England: Pearson.

Jensen, J., 2015: Introductory Digital Image Processing: A Remote Sensing Perspective (4 ed.). Upper Saddle River, NJ, US: Prentice Hall Press.

Jiménez-Muñoz, J. C., Sobrino, J. A., Cristóbal, J., Sòria, G., Ninyerola, M., Pons, X., . . ., and *Mattar, C.*, 2010: Land surface temperature retrieval from historical LANDSAT data. *Revista de Teledetección, 33*, 53–63.

Jiménez-Muñoz, J., Sobrino, J., Skokovic, D., Mattar, C., and *Cristóbal, J.*, 2014: Land Surface Temperature Retrieval Methods From Landsat-8 Thermal Infrared Sensor Data. *IEEE Geosci. and Remote Sens. Lett. 11*(10), 1840–1843. https://doi.org/10.1109/LGRS.2014.2312032

Karnieli, A., Ben-Dor, E., Bayarjargal, Y., and *Lugasi, R.*, 2004: Radiometric saturation of Landsat-7 ETM+ data over the Negev Desert (Israel): problems and solutions. *Int. J. Appl. Earth Observ. Geoinform. 5*(3), 219–237. https://doi.org/10.1016/j.jag.2004.04.001

Kikon, N., Singh, P., Singh, S. K., and *Vyas, A.*, 2016: Assessment of urban heat islands (UHI) of Noida City, India using multi-temporal satellite data. *Sustain. Cities Society 22*, 19–28. https://doi.org/10.1016/j.scs.2016.01.005

Kis, A., Pongrácz, R., Bartholy, J., Gocic, M., Milanovic, M., and *Trajkovic, S.*, 2020: Multi-scenario and multi-model ensemble of regional climate change projections for the plain areas of the pannonian basin. *Időjárás 124*, 157–190. https://doi.org/10.28974/idojaras.2020.2.2

Kovács, K.D., 2019: Evaluation of burned areas with SENTINEL-2 using SNAP. The case of Kineta and Mati, Greece, July 2018. *Geographia Technica, 14*(2), 20–38. https://doi.org/10.21163/GT_2019.142.03

Lau, H., Khosrawipour, V., Kocbach, P., Mikolajczyk, A., Schubert, J., Bania, J., and *Khosrawipour, T.*, 2020: The positive impact of lockdown in Wuhan on containing the COVID-19 outbreak in China. *J. Travel Medicine, 27*(3), 1–7. https://doi.org/10.1093/jtm/taaa037

Lee, D.O., 1984: Urban climates. *Progr. Phys. Geography: Earth Environ 8*(1), 1–31. https://doi.org/10.1177/030913338400800101

Li, L., Tan, Y., Ying, S., Yu, Z., Li, Z., and *Lan, H.*, 2014: Impact of land cover and population density on land surface temperature: case study in Wuhan, China. *J. Appl. Remote Sens. 8*(1), 084993. https://doi.org/10.1117/1.JRS.8.084993

Li, X., Li, W., Middel, A., Harlan, S., Brazel, A. J., and *Turner, B.*, 2016: Remote sensing of the surface urban heat island and land architecture in Phoenix, Arizona: Combined effects of land composition and configuration and cadastral-demographic-economic factors. *Remote Sens. Environ. 174*, 233–243. https://doi.org/10.1016/j.rse.2015.12.022

Lin, C., Lau, A.K., Fung, J.C., Guo, C., Chan, J.W., Yeung, D.W., . . ., and *Lao, X.Q.*, 2020: A mechanism-based parameterisation scheme to investigate the association between transmission rate of COVID-19 and meteorological factors on plains in China. *Sci. Total Environ. 737*(140348). https://doi.org/10.1016/j.scitotenv.2020.140348

Liu, J., Zhou, J., Yao, J., Zhan, X., Li, L., Xu, X., . . ., and *Zhang, K.*, 2020: Impact of meteorological factors on the COVID-19 transmission: A multi-city study in China. *Sci. Total Environ. 726*(138513). https://doi.org/10.1016/j.scitotenv.2020.138513

Ma, Y., Zhao, Y., Liu, J., He, X., Wang, B., Fu, S., . . ., and *Luo, B.*, 2020: Effects of temperature variation and humidity on the death of COVID-19 in Wuhan, China. *Sci. Total Environ. 724*(138226). https://doi.org/10.1016/j.scitotenv.2020.138226

Maithani, S., Nautiyal, G., and *Sharma, A.*, 2020: Investigating the Effect of Lockdown During COVID-19 on Land Surface Temperature: Study of Dehradun City, India. *J. Indian Soc. Remote Sens. 48*(9), 1297–1311. https://doi.org/10.1007/s12524-020-01157-w

Mallick, J., Rahman, A., and *Singh, C. K.*, 2013: Modeling urban heat islands in heterogeneous land surface and its correlation with impervious surface area by using night-time ASTER satellite data in highly urbanizing city, Delhi-India. *Adv. Space Res. 52*(4), 639–655. https://doi.org/10.1016/j.asr.2013.04.025

Mallick, J., Singh, C. K., Shashtri, S., Rahman, A., and *Mukherjee, S.*, 2012: Land surface emissivity retrieval based on moisture index from LANDSAT TM satellite data over heterogeneous surfaces of Delhi city. *Int. J. Appli. Earth Observ. Geoinform. 19*, 348–358. https://doi.org/10.1016/j.jag.2012.06.002

Mathew, A., Khandelwal, S., and *Kaul, N.*, 2016: Spatial and temporal variations of urban heat island effect and the effect of percentage impervious surface area and elevation on land surface temperature: Study of Chandigarh city, India. *Sustain. Cities Soc. 26*, 264–277. https://doi.org/10.1016/j.scs.2016.06.018

Mathew, A., Khandelwal, S., and *Kaul, N.*, 2017: Investigating spatial and seasonal variations of urban heat island effect over Jaipur city and its relationship with vegetation, urbanization and elevation parameters. *Sustain. Cities Soc. 35*, 157–177. https://doi.org/10.1016/j.scs.2017.07.013

Matthews, T., 2012: Heat islands: understanding and mitigating heat in urban areas. *Australian Planner 49*(4), 363–364. https://doi.org/10.1080/07293682.2011.591742

Meng, C., and *Dou, Y.*, 2016: Quantifying the Anthropogenic Footprint in Eastern China. *Sci. Reports 6*(24337), 1–7. https://doi.org/10.1038/srep24337

Mohamadi, B., Chen, S., Balz, T., Gulshad, K., and *McClure, S. C.*, 2019: Normalized Method for Land Surface Temperature Monitoring on Coastal Reclaimed Areas. *Sensors 19*(22), 4836. https://doi.org/10.3390/s19224836

Mukherjee, S., Joshi, P. K., and *Garg, R. D.*, 2017: Analysis of urban built-up areas and surface urban heat island using downscaled MODIS derived land surface temperature data. *Geocarto Int. 32*(8), 900-918. https://doi.org/10.1080/10106049.2016.1222634

Nagy, G., Kovács, R., Szőke, S., Bökfi, K.A., Gurgenidze, T., and Sahbeni, G., 2020: Characteristics of pollutants and their correlation to meteorological conditions in Hungary applying regression analysis. *Időjárás 124*, 113–127. https://doi.org/10.28974/idojaras.2020.1.6

Ndossi, M.I., and *Avdan, U.,* 2016: Application of Open Source Coding Technologies in the Production of Land Surface Temperature (LST) Maps from Landsat: A PyQGIS Plugin. *Remote Sens. 8*(5), 1–31. https://doi.org/10.3390/rs8050413

Nijssen, B., O'donnell, G.M., Hamlet, A.F., and Lettenmaier, D.P., 2001: Hydrologic sensitivity of global rivers to climate change. *Climatic Change 50*, 143–175. https://doi.org/10.1023/A:1010616428763

Offerle, B., Grimmond, C. S., Fortuniak, K., Kłysik, K., and *Oke, T. R.*, 2006: Temporal variations in heat fluxes over a central European city centre. *Theor. Appl. Climatol. 84*(1), 103–115. https://doi.org/10.1007/s00704-005-0148-x

Oke, T. R., 1982: The energetic basis of the urban heat island. *Quart. J. Roy. Meteorol. Soc. 108*(455), 1–24. https://doi.org/10.1002/qj.49710845502

Ord, J. K., and *Getis, A.*, 1995: Local Spatial Autocorrelation Statistics: Distributional Issues and an Application. *Geograph. Anal. 27*(4), 286–306. https://doi.org/10.1111/j.1538-4632.1995.tb00912.x

Patel, H., Talbot, N., Salmond, J., Dirks, K., Xie, S., and *Davy, P.*, 2020: Implications for air quality management of changes in air quality during lockdown in Auckland (New Zealand) in response to the 2020 SARS-CoV-2 epidemic. *Sci. Total Environ. 746*(141129). https://doi.org/10.1016/j.scitotenv.2020.141129

Quattrochi, D. A., and *Luvall, J. C.*, 2004: Thermal Remote Sensing in Land Surface Processes. Boca Raton, Florida, US: CRC Press. https://doi.org/10.1201/9780203502174

Ranagalage, M., Dissanayake, D., Murayama, Y., Zhang, X., Estoque, R., Perera, E., and *Morimoto, T.*, 2018: Quantifying Surface Urban Heat Island Formation in the World Heritage Tropical Mountain City of Sri Lanka. *ISPRS Int. J. Geo-Inf., 7*(9), 341. https://doi.org/10.3390/ijgi7090341

Riaño, D., Salas, J., and *Chuvieco, E.*, 2000: Corrección Atmosférica y Topográfica, Información Multi-temporal y Auxiliar Aplicadas a la Cartografía de Modelos de Combustibles con Imágenes Landsat-TM, In: Tecnologías geográficas para el desarrollo sostenible (eds. Aguado, I., and Gómez, M.). Madrid, Comunidad de Madrid, España: Universidad de Alcalá: Asociación Española de Geografía, 222–239. (In Spain)

Rozenstein, O., Qin, Z., Derimian, Y., and *Karnieli, A.*, 2014: Derivation of Land Surface Temperature for Landsat-8 TIRS Using a Split Window Algorithm. *Sensors 14*(4), 5768–5780. https://doi.org/10.3390/s140405768

Sahana, M., Ahmed, R., and *Sajjad, H.*, 2016: Analyzing land surface temperature distribution in response to land use/land cover change using split window algorithm and spectral radiance model in Sundarban Biosphere Reserve, India. *Modeli. Earth Syst. Environ. 2*(81), 1–11. https://doi.org/10.1007/s40808-016-0135-5

Sattari, F., and *Hashim, M.*, 2014: A Breife Review of Land Surface Temperature Retrieval Methods from Thermal Satellite Sensors. *Middle East J. Sci. Res. 22*(5), 757–768. https://doi.org/10.5829/idosi.mejsr.2014.22.05.21934

Sekertekin, A., and *Bonafoni, S.*, 2020: Land Surface Temperature Retrieval from Landsat 5, 7, and 8 over Rural Areas: Assessment of Different Retrieval Algorithms and Emissivity Models and Toolbox Implementation. *Remote Sensing 12*(2), 294. https://doi.org/10.3390/rs12020294

Sellers, P. J., 1985: Canopy reflectance, photosynthesis and transpiration. *Int. J.Remote Sens. 6*(8), 1335–1372. https://doi.org/10.1080/01431168508948283

Shahmohamadi, P., Che-Ani, A. I., Maulud, K. N., Tawil, N. M., and *Abdullah, N. A.*, 2011: The Impact of Anthropogenic Heat on Formation of Urban Heat Island and Energy Consumption Balance. *Urban Studies Res. 2011*(497524), 1–9. https://doi.org/10.1155/2011/497524

Singh, P., Kikon, N., and *Verma, P.*, 2017: Impact of land use change and urbanization on urban heat island in Lucknow city, Central India. A remote sensing based estimate. *Sustainable Cities and Society, 32*, 100-114. https://doi.org/10.1016/j.scs.2017.02.018

Singh, V., Singh, S., Biswal, A., Kesarkar, A. P., Mor, S., and *Ravindra, K.*, 2020: Diurnal and temporal changes in air pollution during COVID-19 strict lockdown over different regions of India. *Environ. Pollut. 266*(115368). https://doi.org/10.1016/j.envpol.2020.115368

Slater, P. N., Biggar, S. F., Holm, R. G., Jackson, R. D., Mao, Y., Moran, M. S., . . ., and *Yuan, B.*, 1987: Reflectance- and radiance-based methods for the in-flight absolute calibration of multispectral sensors. *Remote Sens. Environ. 22*(1), 11–37. https://doi.org/10.1016/0034-4257(87)90026-5

Sobrino, J. A., and *Romaguera, M.*, 2004: Land surface temperature retrieval from MSG1-SEVIRI data. *Remote Sens. Environ. 92*(2), 247–254. https://doi.org/10.1016/j.rse.2004.06.009

Sobrino, J. A., Jiménez-Muñoz, J. C., and *Paolini, L.*, 2004: Land surface temperature retrieval from LANDSAT TM 5. *Remote Sens. Environ. 90*(4), 434-440. https://doi.org/10.1016/j.rse.2004.02.003

Sobrino, J., Raissouni, N., Kerr, Y., Olioso, López García, M., Belaid, . . ., and *Dempere-Marco, L.*, 2000: *Teledetección* (1 ed.). Valencia, Comunidad Valenciana, Spain: Universidad de Valencia.

Soleimani Vosta Kolaei, F., and *Akhoondzadeh, M.,* 2018: A comparison of four methods for extracting Land Surface Emissivity and Temperature in the Thermal Infrared Hyperspectral Data. *Earth Observ. Geomatics Engin. 2*(1), 56–63. doi:10.22059/eoge.2018.239666.1011

Tobías, A., Carnerero, C., Reche, C., Massagué, J., Via, M., Minguillón, M. C., . . ., and Querol, X., 2020: Changes in air quality during the lockdown in Barcelona (Spain) one month into the SARS-CoV-2 epidemic. *Sci. Total Environ. 726*(138540). https://doi.org/10.1016/j.scitotenv.2020.138540

Tran, D. X., Pla, F., Latorre-Carmona, P., Myint, S. W., Caetano, M., and *Kieu, H. V.*, 2017: Characterizing the relationship between land use land cover change and land surface temperature. *ISPRS J. Photogram. Remote Sens. 124*, 119–132. https://doi.org/10.1016/j.isprsjprs.2017.01.001

Ursu, C-D., 2019: The land surface temperature evolution (LST) using LANDSAT scenes. Case study: The industrial platform Săvineşti. *Geographia Technica 14*(2), 131–142. https://doi.org/10.21163/GT_2019.142.12

Valor, E., and *Caselles, V.*, 1996: Mapping land surface emissivity from NDVI: Application to European, African, and South American areas. *Remote Sens. Environ. 57*(3), 167–184. https://doi.org/10.1016/0034-4257(96)00039-9

Vlassova, L., Perez-Cabello, F., Nieto, H., Martín, P., Riaño, D., and *Riva, J. d.*, 2014: Assessment of Methods for Land Surface Temperature Retrieval from Landsat-5 TM Images Applicable to MultiscaleTree-Grass Ecosystem Modeling. *Remote Sens. 6*(5), 4345–4368. https://doi.org/10.3390/rs6054345

Walawender, J. P., Szymanowski, M., Hajto, M. J., and *Bokwa, A.*, 2014: Land Surface Temperature Patterns in the Urban Agglomeration of Krakow (Poland) Derived from Landsat-7/ETM+ Data. *Pure Appl. Geophys. 171*(6), 913–940. https://doi.org/10.1007/s00024-013-0685-7

Wan, Z., 2013: *C*ollection-6 MODIS Land Surface Temperature Products Users' Guide. Retrieved 12 16, 2020, from Land Processes Distributed Active Archive Center (LP DAAC): https://lpdaac.usgs.gov/documents/118/MOD11_User_Guide_V6.pdf

Wang, Y., Zhan, Q., and *Ouyang, W.*, 2017: Impact of Urban Climate Landscape Patterns on Land Surface Temperature in Wuhan, China. *Sustainability 9*(10), 1700. https://doi.org/10.3390/su9101700

Wang, Z.-H., and *Upreti, R.*, 2019: A scenario analysis of thermal environmental changes induced by urban growth in Colorado River Basin, USA. *Landscape Urban Plan. 181*, 125–138. doi:10.1016/j.landurbplan.2018.10.002

Weng, Q., 2019: Land Surface Temperature Data Generation. In (Ed. *Q. Weng*) Techniques and Methods in Urban Remote Sensing (1 ed.) The Institute of Electrical and Electronics Engineers Press. 91–127. https://doi.org/10.1002/9781119307303.ch5

Xiao, R. B., Ouyang, Z. Y., Zheng, H., Li, W. F., Schienke, E. W., and *Wang, X. K.*, 2007: Spatial pattern of impervious surfaces and their impacts on land surface temperature in Beijing, China. *J. Environ. Sci. 19*(2), 250–256. https://doi.org/10.1016/S1001-0742(07)60041-2

Xie, J., and Zhu, Y., 2020: Association between ambient temperature and COVID-19 infection in 122 cities from China. *Sci. Total Environ. 724*(138201). https://doi.org/10.1016/j.scitotenv.2020.138201

Xu, H., 2015: Retrieval of the reflectance and land surface temperature of the newly-launched Landsat 8 satellite. *Chinese J. Geophys. 58*(3), 741–747. doi:10.6038/cjg20150304

Xu, H., Lin, D., and *Tang, F.*, 2012: The impact of impervious surface development on land surface temperature in a subtropical city: Xiamen, China. *Int. J. Climatol. 33*(8), 1873–1883. https://doi.org/10.1002/joc.3554

Yoo, C., Im, J., Park, S., and *Cho, D.*, 2017: Thermal Characteristics of Daegu using Land Cover Data and Satellite-derived Surface Temperature Downscaled Based on Machine Learning. *Korean J. Remote Sens. 33*, 1101–1118.

Yu, X., Guo, X., and *Wu, Z.*, 2014: Land Surface Temperature Retrieval from Landsat 8 TIRS—Comparison between Radiative Transfer Equation-Based Method, Split Window Algorithm and Single Channel Method. *Remote Sens. 6*(10), 9829–9852. https://doi.org/10.3390/rs6109829

Yuan, F. and *Bauer, M. E.*, 2007: Comparison of impervious surface area and normalized difference vegetation index as indicators of surface urban heat island effects in Landsat imagery. *Remote Sens. Environ. 106*(3), 375–386. https://doi.org/10.1016/j.rse.2006.09.003

Zhan, Q., Meng, F., and *Xiao, Y.*, 2015: Exploring the relationships of between land surface temperature, ground coverage ratio and building volume density in an urbanized environment. *Int. Arch. Photogramm. Remote Sens. Spatial Inf. Sci.*, *XL-7/W3*, 255–260. https://doi.org/10.5194/isprsarchives-XL-7-W3-255-2015

Zsebeházi, G. and *Szépszó, G.*, 2020: Modeling the urban climate of Budapest using the SURFEX land surface model driven by the ALADIN-climate regional climate model results. *Időjárás 124*, 191–207. https://doi.org/10.28974/idojaras.2020.2.3